Applied Surface Science 575 (2022) 151751

Contents lists available at ScienceDirect

Applied Surface Science

journal homepage: www.elsevier.com/locate/apsusc

Full Length Article

Selectivity in atomically precise etching: Thermal atomic layer etching of a CoFeB alloy and its protection by MgO

Mahsa Konh [a], Yang Wang [b], Hang Chen [b], Subhash Bhatt [b], John Q. Xiao [b], Andrew V. Teplyakov [a,*]

[a] University of Delaware, Department of Chemistry and Biochemistry, Newark, DE, USA
[b] University of Delaware, Department of Physics and Astronomy, Newark, DE, USA

ARTICLE INFO

Keywords:
Atomic layer etching
Selectivity in etching
Reaction mechanism
XPS
Thermal desorption

ABSRACT

The central unit in an integrated memory device is a magnetic tunnel junction (MTJ) consisting of two ferromagnetic layers, often using complex alloys such as CoFeB, separated by an insulating barrier such as MgO. Atomic level precision is required to fabricate miniaturized devices, and atomic layer etching (ALE) is one of the most promising methods to do this. However, at the nanoscale, it is imperative to maintain the concentration of each element in an alloy during etching, and it is important to not affect the insulating barrier, i.e. the etching process should stop at MgO. Here we use thermal dry etching of CoFeB alloy thin films with sequential doses of chlorine and 2,4-pentanedione (acetylacetone, acacH). Patterned samples are modified with atomic level precision, and the process is completely selective to the removal of CoFeB alloy in ALE regime without changing the alloy composition and without etching MgO that is used as a protecting layer. The etching process was investigated by comparing the film thickness on a patterned surface before and after ALE process using atomic force microscopy (AFM). The viable key features of the reaction mechanism were proposed by detection of key desorbing fragments during a heating ramp via temperature-programmed desorption (TPD) experiments. *Ex-situ* X-ray photoelectron spectroscopy (XPS) was performed to characterize the surface during ALE process.

1. Introduction

The atomically precise manufacturing is quickly becoming a reality. With a recent unveiling of the technology for 2 nm chip manufacturing [1], atomically-precise devices clearly make it into the realm of accessible products. With these breakthroughs, the device features and the overall properties of the corresponding multilayer constructs have to be manipulated at the scale where chemical transformations and surface processes have to be understood at the highest possible levels of precision.

One of the booming examples of these technologies is atomic layer etching (ALE) [2–5], and specifically, atomic processing of magnetic materials, with applications in magnetic tunnel junctions for magnetic random-access memory and logic devices, and neuromorphic computers [6–9]. There, the ferromagnetic layers are commonly made of metallic alloys, and CoFeB is a critical material in these devices. Recent work has addressed the mechanisms of ALE of pure iron [10,11] and cobalt [12–14] films, and the possibility of ALE for this alloy has been reported [15]. However, for features and thin films in the nanometer scale range, mechanistic understanding of the process is imperative, as the subtleties of etching process may leave the surface of the films enriched in some elements or remove desired additives, particularly boron.

The general approach to achieve ALE regime in thin metallic films is oxidation or chlorination as the first step of the process followed by the removal of metal-containing product by adding an organic ligand such as formate, carboxylate, acetylacetonate (acac), or hexafluoroacetylacetonate (hfac). Acetylacetonate ligands have been demonstrated to be efficient in helping the removal of a wide variety of metals, including Cu [16–18], Ru [18], Co [12–14], Pt [19], Fe [10,11], Pb [20] and many others [18]. The first step of this ALE process can be controlled kinetically (direct chlorination with Cl_2 [10–13], SO_2Cl_2 [21] or WCl_6 [22] as chlorinating etchant), and the second step could be driven thermodynamically by producing stable volatile metal-containing molecules leading to a true atomically-limited process.

The process of metal oxidation or chlorination can be quite complex and the control can be achieved by thermal processing [23], plasma

* Corresponding author.
E-mail address: andrewt@udel.edu (A.V. Teplyakov).

https://doi.org/10.1016/j.apsusc.2021.151751
Received 13 September 2021; Received in revised form 15 October 2021; Accepted 27 October 2021
Available online 31 October 2021

[24], or UV means [25]. The removal of metal-containing volatile products could also involve multiple processing steps and methods [22,23,25], and that is why rationalizing mechanistic investigations of the process is so difficult. The traditional way of using quartz microbalance quantification [26–28] and ex situ post-characterization with X-ray photoelectron spectroscopy (XPS) and other surface analytical techniques [11–13,29] can only provide a snapshot of ALE. However, kinetic analysis with temperature-dependent investigations using mass spectrometry for direct quantification of desorbing products [10,12,26] has recently become a much more advanced method of kinetic characterization of ALE *in-situ* and can now provide direct insight that can be modelled computationally. That last aspect is especially important for the simulation of the ALE process. The recent work on interaction of organic ligands with surfaces of nickel [30], copper [24], ruthenium [25], cobalt [31] rarely predicts the correct outcome of ALE if only thermodynamically stable stationary points are investigated. However, the role of monodentate ligands has been suggested to play a role in ALE of iron [10], and this is the approach that can benefit tremendously from direct *in-situ* measurements.

An additional and very important property of the ALE process is a possibility to selectively remove controlled layers of one material without affecting another, if appropriate chemical process is selected [32]. For example, the central unit in an integrated memory device is a magnetic tunnel junction consisting of two ferromagnetic layers, often using CoFeB, separated by an insulating barrier such as MgO. Thus, in designing processing for a real device, it is extremely important to selectively etch the alloy with atomic precision and at the same time not to affect (stop the process at) the MgO layers. As will be demonstrated below, the chemistry of the process can be designed to selectively remove only one material but not affect the other, opening the future opportunities for combinatorial approach in designing ALE processes.

The key questions that need to be addressed in the mechanistic studies in addition to the identification of metal-containing volatile products are the thermal removal of by-products (water, HCl, etc) and also the chemistry that allows for the removal of light elements, such as boron in CoFeB alloy. The key problems that have to be resolved at the nanoscale are whether it is possible to maintain the composition of the CoFeB alloy during the etching process and whether it is possible to completely stop the process by protecting the alloy with a very thin layer (a few nanometers) of MgO.

These issues will be addressed in this work by achieving and confirming the ALE regime for the patterned CoFeB samples, investigating the desorption of the ALE products with thermal desorption, assessing the composition of the resulting surfaces with *in-situ* Auger electron spectroscopy (AES) and *ex-situ* X-ray photoelectron spectroscopy (XPS), and analyzing the changes in the topography of the patterned films with atomic force microscopy (AFM). Although AFM was used previously to evaluate etching process on a masked MoS_2 sample [33], it is the first time that this technique is applied on a patterned sample with various films deposited on it to measure the thickness of each material precisely and simultaneously.

2. Experimental section

2.1. Samples and compounds used.

The CoFeB alloy films used in this study were deposited with DC power on thermally oxidized silicon wafer at room temperature in a home-built magnetron sputtering system. The CoFeB alloy targets were commercially purchased (ACI Alloys, Inc.), and the surface elemental composition of the deposited samples was evaluated by *ex-situ* XPS. The base pressure of the chamber was 1.4×10^{-7} Torr and the deposition atmosphere was 4.5 mTorr argon gas. The MgO capping layer was deposited with RF power and the MgO-capped samples have an extra 0.5-nm thick Ti layer underneath CoFeB to promote adhesion. The deposition rates of the films were calibrated by X-ray reflectivity measurements. The stripe- and cross-shaped films were patterned using a lift-off photolithography technique. To create sharp edges for the films, bilayer photoresists (LOR/AZ1512) were employed to achieve an undercut profile. During ALE experiments, molecular chlorine gas was dosed into the UHV chamber using a home-built solid-state electrochemical cell based on silver chloride. Cadmium chloride was also used in this cell to increase the defect concentration and allow the cell to work continuously for extended periods of time. The sample surface chlorine saturation within the experimental conditions used in this work was confirmed by AES. 2,4-pentanedione (acetylacetone, acacH) (99.5%, Aldrich) was introduced into the chamber through leak valves after several freeze–pump-thaw cycles. The purity of the compound was confirmed *in-situ* by mass spectrometry.

2.2. Reactor, thermal desorption investigation, and etch rate determination.

The produced samples were mounted on a sample holder in the ultra-high vacuum (UHV) chamber with a base pressure of 10^{-9} Torr. This UHV chamber is equipped with a differentially pumped mass spectrometer (Hiden Analytical) that can detect mass-to-charge ratios up to 510 amu. The samples were attached to a button heater with a tantalum collar inside the UHV chamber. Each sample was annealed at 440 K for 40 min to remove physisorbed contaminants. The predetermined amount of acacH was dosed into the chamber via a leak valve and predetermined amount of chlorine was dosed using a solid-state electrochemical cell at desired sample temperature monitored by a thermocouple attached to the tantalum shield of the sample holder.

Two different types of experiments are described below:

1) For thermal desorption experiments, following the dose of acacH and/or chlorine, the temperature of the sample was lowered to approximately room temperature. During the thermal desorption, the temperature of the sample was increased linearly at a rate of 2 K/s up to 710 K controlled by a dedicated temperature controller (Eurotherm, Model 818). The desorbing fragments were detected by the mass spectrometer. The studies presented target chlorine-containing fragments with ^{35}Cl isotope. Following the predetermined set of thermal desorption studies, each sample was removed from the set-up for final characterization and then replaced with a new sample.
2) For multicycle ALE experiments, one CoFeB alloy ALE cycle consisted of chlorination at 440 K for 40 min followed by 300 L acacH exposure. Up to 30 cycles were performed in order to determine the CoFeB alloy etch rate. These samples were never heated above 440 K and never reused.

2.3. Sample characterization

Auger electron spectroscopy (ESA 100, STAIB Instruments Inc.) was used to confirm the surface composition before and after the *in-situ* thermal etching experiments.

Surface chemical characterization was performed *ex-situ* by XPS on a K-alpha+ XPS system from Thermo Scientific in the Surface Analysis Facility at the University of Delaware using Al K-alpha X-ray source ($h\nu = 1486.6$ eV) at a 35.3° takeoff angle with respect to the analyzer. High-resolution spectra were collected over the range of 20 eV at 0.1 eV/step with the pass energy of 20 eV. The survey spectra were collected over the energy range of 0–1000 eV. CasaXPS (version 2.3.16) software was utilized to analyze all data [34]. To calibrate the XPS scale, carbon peak was set at 284.6 eV. Mapping mode was performed with spot step size of 100 μm. Survey spectra were collected over the binding energy range of 0 to 3150 eV for 5.78×5.92 mm^2 surface area. The image was processed with Avantage software (version 5.9911).

Atomic force microscopy (AFM) images were acquired under tapping mode with a J-scanner scanning probe microscope (Multimode,

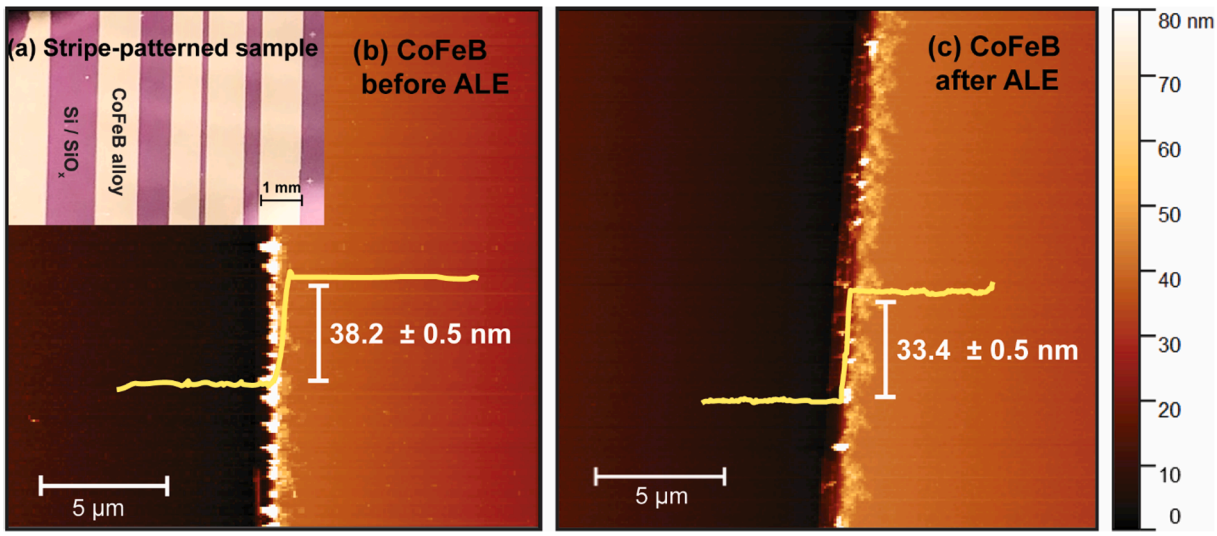

Fig. 1. (a) Photograph of the stripe-patterned CoFeB sample (light areas represent thin film stripes of CoFeB alloy of approximately 38 nm thickness as determined by X-ray reflectivity, dark areas correspond to the underlying substrate, native oxide on a silicon wafer); AFM images of patterned CoFeB alloy sample (b) before 30 ALE cycles, and (c) after 30 ALE cycles. Representative line profiles of the step edges are provided with the corresponding height recorded before and after ALE.

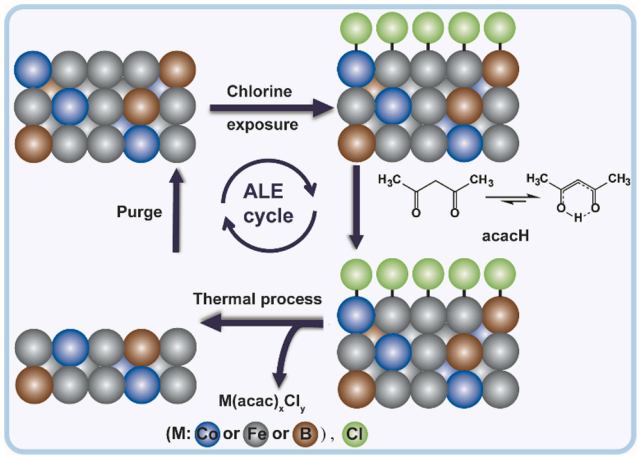

Scheme 1. Proposed ALE mechanism for CoFeB etching via chlorine followed by acacH exposure.

NanoScope V). The sensing tips (aluminum coated, BudgetSensors) have a resonant frequency of 300 kHz and a 40 N/m force constant. The images were processed with Gwyddion software.

Small-angle X-ray reflectivity (XRR) [35] measurements was used to calibrate the thicknesses of the as-deposited CoFeB films. During the measurement, X-rays produced by a copper K-α radiation source were incident on the film at small angles ($0.6 < 2 < 6$), and the reflected photons were counted by the detector. The peak oscillation period and decay rate can yield information about the film thickness and surface roughness, respectively. After measurement, the raw data were fitted with the GenX software [36]. Representative result of a deposition rate calibration is shown in Figure S1 of the Supporting Information section.

As an independent method to calibrate the ALE etch rate, we deposited a CoFeB film, carried out 30 cycles ALE experiments, and confirmed the film thickness before and after ALE by XRR measurement. As shown in Figure S2 of the Supporting Information section, within experimental uncertainties, the etch rate (6.1 ± 0.6 nm) obtained from XRR agrees well with that obtained by AFM, as described in detail below.

3. Results and discussion

High-quality CoFeB alloy films were deposited on thermally oxidized silicon wafers by magnetron sputtering and patterned with the lift-off photolithography technique (see section 2.1 for specific details).

3.1. Confirming ALE of CoFeB alloy with AFM

CoFeB alloy ALE by sequential exposure to chlorine and acacH were examined using AFM images on the patterned sample with five CoFeB film stripes deposited on silicon wafer, as shown in Fig. 1. The chlorine exposure was chosen based on the saturation of AES intensity of the chlorine signal as a function of dosing time. The dose of acacH was chosen to be 300 L, as an exposure more than sufficient to saturate a monolayer at the conditions used based on the previous work [10,12]. The vacuum chamber was evacuated to its base pressure after each dose. The ALE temperature of 440 K was chosen based on the previously optimized ALE procedures for cobalt [12] and iron [10]. These prior studies also confirmed that chlorination is required for ALE of both cobalt and iron within the temperature interval investigated. The thickness of each stripe measured by AFM before and after 30 cycles of ALE is shown in Fig. 1, and it was assumed that the underlying substrate (native oxide on a silicon wafer) was not etched by the procedure. This last assumption is supported by the well-known requirements for silica surface ALE described in literature [4,37] and by the recently published investigation on silica etching [38]. The thickness reported on the representative line profiles in Fig. 1 is the average thickness measured among all five stripes of the same sample. The average thickness etched from the sample was measured to be 4.5 ± 0.7 nm after 30 cycles, resulting in 0.15 nm/cycle etch rate at these optimized conditions. The thickness change after 15 cycles with the same conditions was ~ 2.5 nm. The small difference in average etching rate for 15 and 30 cycles determined by AFM is likely explained by the initial (oxidized) surface of the alloy that would be expected to affect the initial etching rate. Nevertheless, the etching process is confirmed, and the regime corresponding to atomic layer removal can be achieved.

3.2. XPS investigation of CoFeB alloy thin films

After establishing that ALE regime can be achieved for the CoFeB films described in this work, the mechanisms of the process could be inferred; however, before thermal desorption could be used to follow the

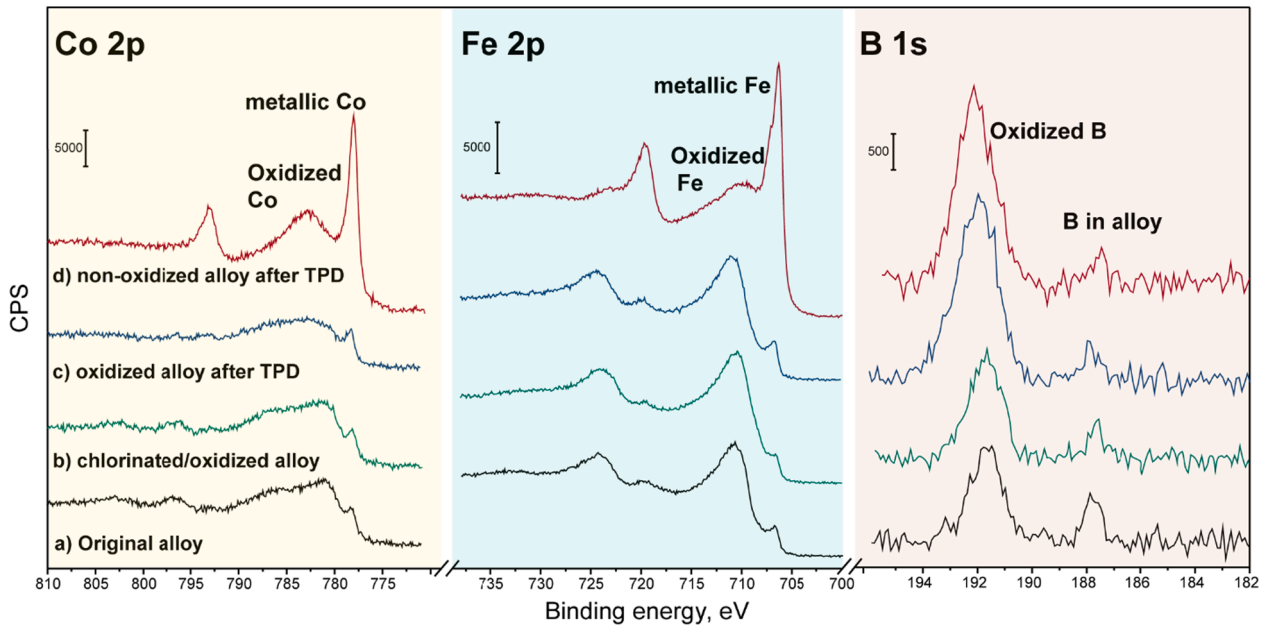

Fig. 2. High resolution XPS investigations of Co 2p, Fe 2p and B 1 s spectral regions for (a) original oxidized alloy, (b) the alloy sample exposed to chlorine at 373 K, and (c) the sample after TPD (heated to 710 K), and (d) non-oxidized (sputter-cleaned) sample after TPD (heated to 710 K).

Table 1
Percent concentration of cobalt, iron, and boron after each etching steps and after 30 ALE cycles for the samples prepared by using standard sputtering targets.

Surface	Treatment	XPS atomic concentration (at. %)		
		Co 2p	Fe 2p	B 1 s
Non-patterned sample	Original alloy	26.5 ± 1.6	53.6 ± 1.0	19.9 ± 2.0
	Chlorinated/oxidized alloy	23.6 ± 1.0	49.6 ± 2.3	28.5 ± 4.5
	Oxidized alloy after TPD	24.9 ± 2.7	54.4 ± 1.5	19.9 ± 4.1
	Non-oxidized alloy after TPD	22.1 ± 1.1	53.0 ± 1.2	24.9 ± 1.8
Stripe-patterned sample	Alloy surface before ALE cycles	16.7 ± 2.2	50.5 ± 2.0	32.8 ± 3.5
	Alloy surface after ALE cycles	16.6 ± 2.7	53.1 ± 2.6	30.3 ± 3.7

temperature-dependent evolution of etching products, it was also necessary to understand how the surface of the alloys under investigation changed during the ALE process, most importantly, whether the composition has changed during ALE. Scheme 1 describes the proposed general approach and viable reactions during CoFeB alloy atomic layer etching cycle using sequential exposure of chlorine and acacH.

In order to uncover chemical changes of the surface, the sample surfaces after chlorination and then after exposure to an organic ligand during ALE process were characterized by XPS. This investigation is summarized in Fig. 2 and Table 1. The key comparison points for these surfaces are a) the starting alloy surface, b) the same surface preheated to 440 K and chlorinated, and exposed to acacH at 440 K (ALE cycle). On the non-patterned sample (Table 1), it is shown that the chemical composition is preserved in one ALE cycle, the composition remained the same even after thermal desorption to 710 K needed for the temperature-programmed experiments described below. On the stripe-patterned sample, the chemical compositions before and after 30 ALE cycles, when each cycle consists of sequential exposure to chlorine and acacH at 440 K, does not appear to be affected by the processing. In other words, these *ex-situ* XPS investigations confirm that Co, Fe, and B elements maintain constant relative concentrations as shown in Table 1 (which is extremely important in practical ALE processes) and that no unusual changes in oxidation states of these elements are recorded after the ALE cycles or even after a TPD experiment. Of course, since these measurements are not conducted *in-situ*, the most important result is that the concentration of each element does not change substantially during this ALE process. Because of low relative intensity, B 1s signal is perhaps less reliable in quantification of the reported concentrations; however, the concentrations of all three main alloy elements remain nearly constant within the error of measurement.

Two more points have to be examined in this section. First, if the alloy surface is cleaned by Ar^+ sputtering in situ and then a full ALE cycle is performed, followed by thermal desorption, the Co-to-Fe ratio is not affected. However, both metals appear to be much more reduced, as evidenced by the observation of a strong peak at 778.2 eV for cobalt (Co $2p_{3/2}$) corresponding to its metallic state and at 706.7 eV for iron (Fe $2p_{3/2}$), corresponding to the 0-oxidation state as well. Second observation concerns the oxidation state of boron. The B 1 s spectra clearly show that for all the surfaces investigated, there are two features: one at 187 eV indicating the elemental boron in an alloy [39] and another at 192 eV corresponding to the oxidized boron on a surface. Of course, boron is easily oxidized when briefly exposed to ambient conditions upon transfer to the XPS instrument. However, even in vacuum conditions used here, surface boron is quickly oxidized. In fact, the B signature in the AES spectra also corresponds to the oxidized state, suggesting that this is the chemical state of this element that should be targeted during ALE processing, especially given that in most ALE systems the base pressure is substantially higher than in the experiments presented here. This will be further used in thermal desorption studies. XPS also confirmed that chlorine was removed from the surface following ALE and thermal desorption, and this is fully consistent with the in-situ Auger electron spectroscopy confirmation of chlorine removal.

3.3. Morphology changes during CoFeB ALE

Another question that has to be addressed before the mechanistic insights into CoFeB alloy ALE can be inferred is the evolution of the sample surface morphology. It is common that the sample surfaces get smooth during ALE [27,40,41], and some mechanistic reasoning for such an effect has been provided [10,42]. AFM measurements of CoFeB

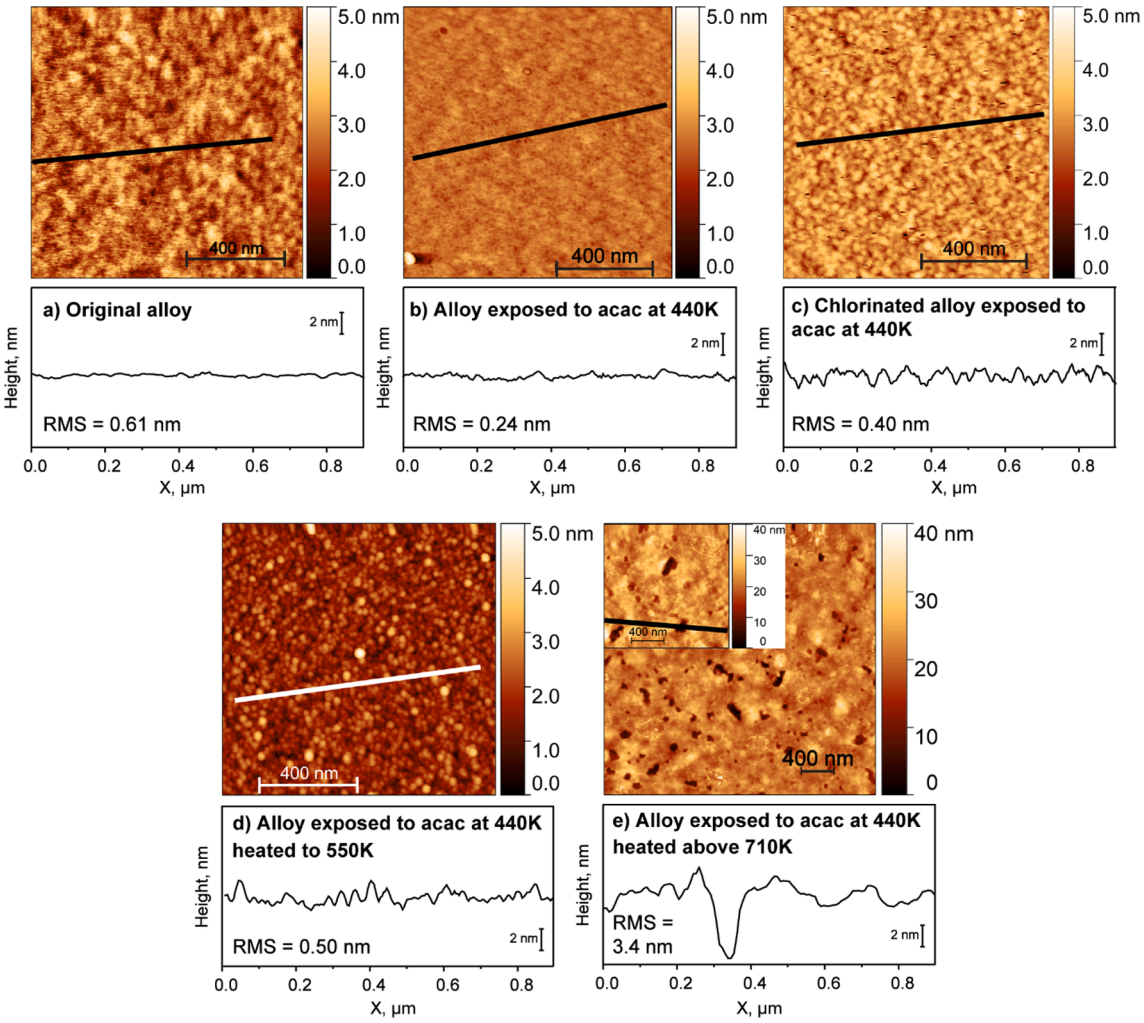

Fig. 3. AFM images of CoFeB alloy films: (a) original alloy film; (b) acacH adsorption at 440 K; (c) chlorinated alloy film exposed to acacH at 440 K; (d) acacH adsorption at 440 K followed by heating to 550 K; (e) acacH adsorption followed by heating above 710 K.

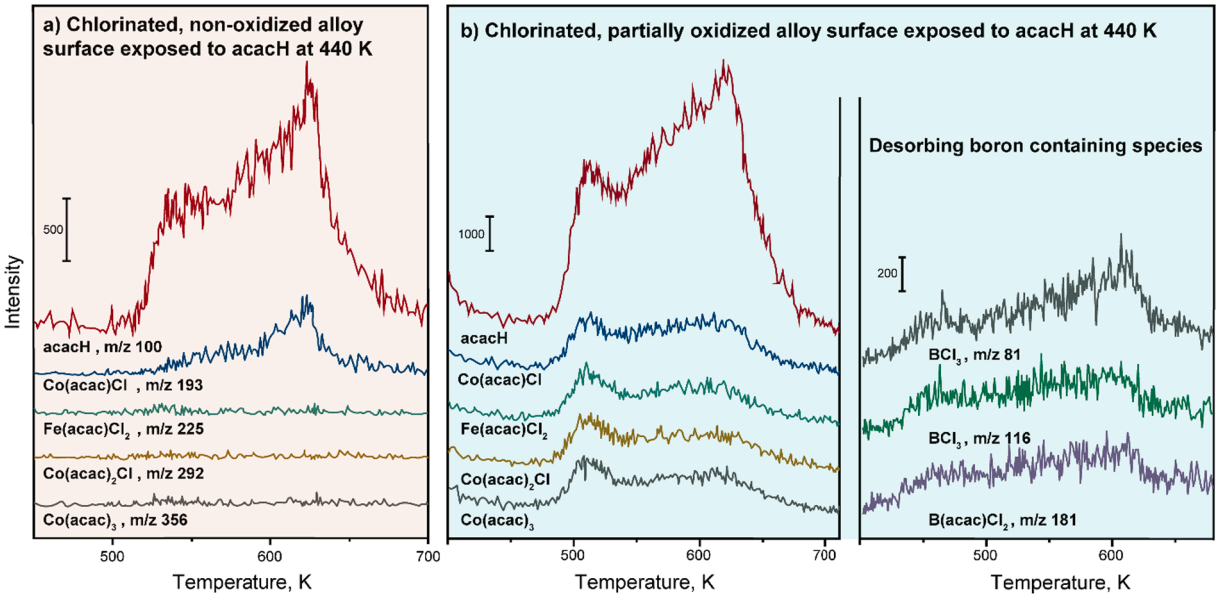

Fig. 4. Summary of TPD studies of (a) chlorinated, non-oxidized alloy surface exposed to acacH at 440 K, and (b) chlorinated, partially oxidized alloy surface exposed to acacH at 440 K.

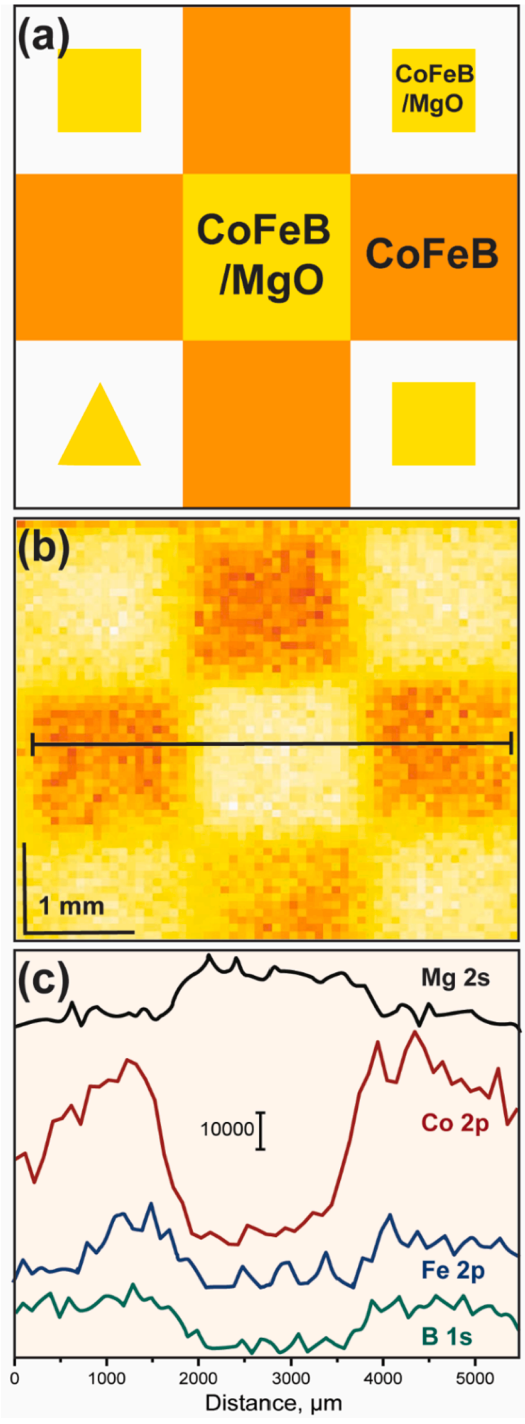

Fig. 5. (a) Schematic illustration, and (b) XPS mapped image of the CoFeB/MgO patterned sample, (c) representative line profiles (offset for clarity) for the regions corresponding to Mg 2s, Co 2p, Fe 2p, and B 1s.

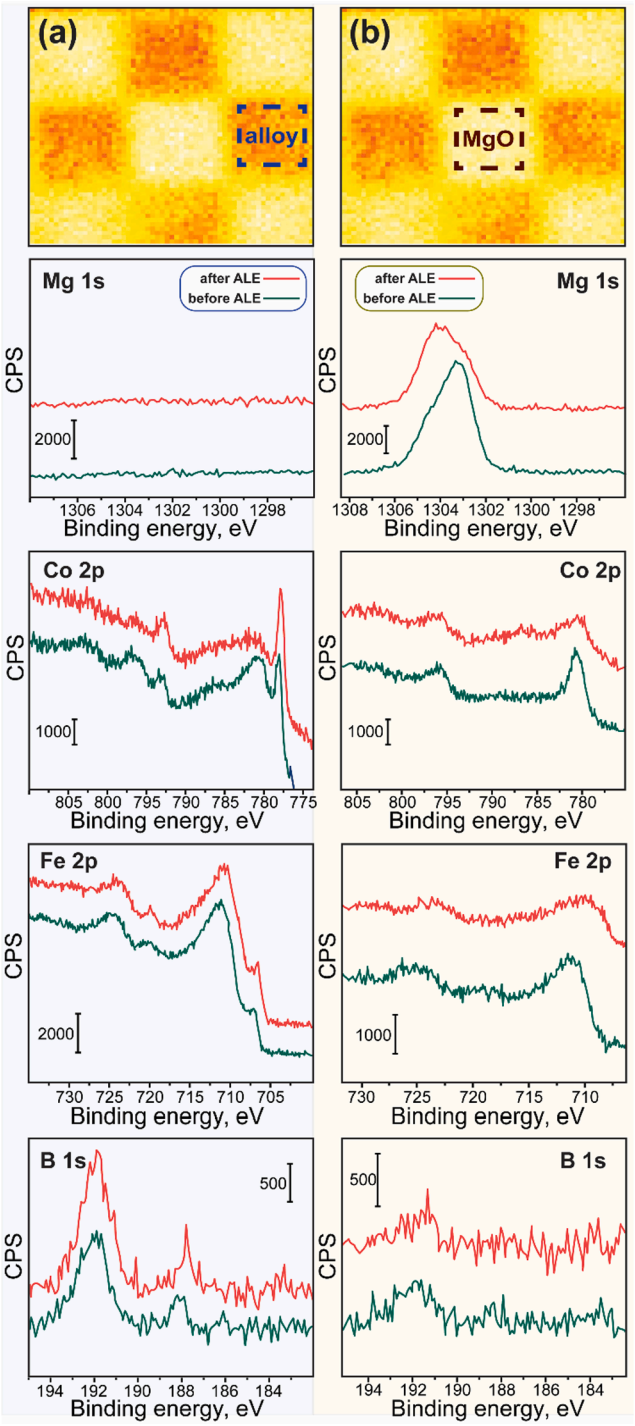

Fig. 6. High resolution XPS spectra collected (a) on the CoFeB alloy feature, and (b) on MgO-protected CoFeB feature indicated in the XPS mapped image shown at the top.

surfaces were used in this work to compare the surface roughness before and after ALE and in each step of the proposed ALE process. The original CoFeB alloy thin film is very smooth to start with (RMS of 0.61 nm, Fig. 3a), so the effect of ALE would not likely be observed as a smoothing but rather as the absence of roughening. The surface roughness does not change noticeably after it is exposed to acacH at 440 K (Fig. 3b). Chlorination does not change the morphology either, and the RMS confirmed that the roughness is still in the range of picometers after acacH exposure on chlorinated surface (Fig. 3c). Only annealing to elevated temperature (more than 710 K) can cause pit formation, which increases the overall RMS to 3.4 nm (Fig. 3e) and this temperature is fully consistent with similar outcomes for cobalt and iron films reported earlier [10,12]. However, if the heating stops below this temperature, no pitting will occur, which will be important in temperature-programmed desorption studies reported below. Fig. 3 also shows the image of the sample surface after ALE process heated to 550 K with no apparent changes in the surface roughness.

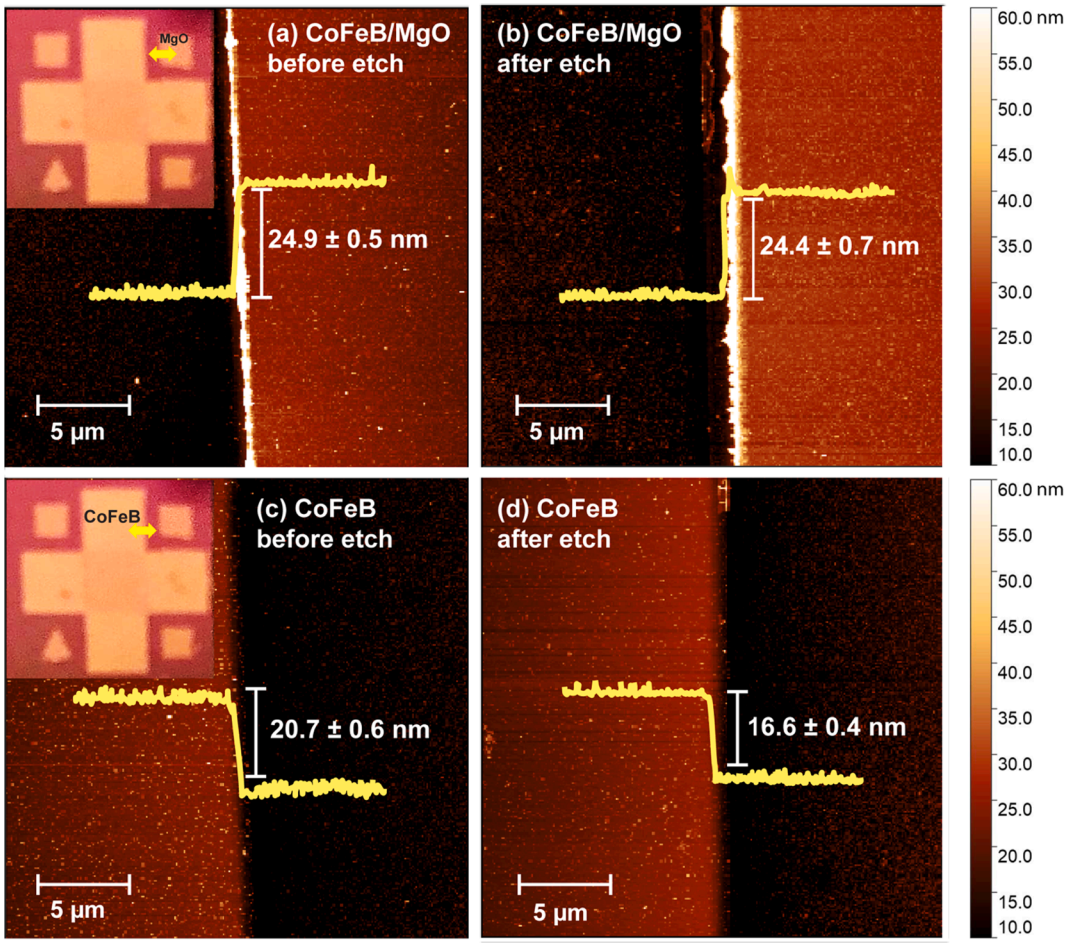

Fig. 7. AFM images of the step at CoFeB/MgO feature (a) before ALE, and (b) after 30 ALE cycles, and at CoFeB feature (c) before ALE, and (d) after 30 ALE cycles. The thickness was measured for the edges of the features marked by arrows on the photograph insets in parts (a) and (c), respectively.

3.4. Thermal desorption investigation

AFM measurements indicate that the CoFeB alloy thin films could be etched with atomic precision and in the ALE regime using sequential doses of chlorine and acacH. Given that the relative surface concentration of the alloy elements and the roughness of the surface are not affected by the ALE process up to 710 K, thermal desorption can be used within this temperature interval to follow the species evolving form the surface. The most complicated part of this analysis is that since TPD was performed after ALE (which required 440 K processing temperature), only some remaining surface species could be recorded by this technique and only if these species are sufficiently volatile. In this work, metal containing products desorbing from pre-chlorinated, partially oxidized and non–oxidized (Ar^+ sputtered) surfaces were followed by a mass spectrometer. Again, since acetylacetone (acacH) was introduced to the surface at 440 K, all the surface species desorbed below this threshold could not be recorded by TPD. Summary of the TPD experiments is presented in Fig. 4. The products were starting to desorb around 500 K on non-oxidized and partially oxidized surfaces. However, if the surface does not contain additional oxygen, only some Co(acac)Cl metal-containing fragments were recorded to desorb above 600 K (a temperature where some desorption was reported for clean cobalt surfaces [12,29]). If the surface contained additional oxygen atoms, a number of fragments containing both cobalt and iron were recorded to desorb well below 550 K. This observation does not necessarily rule out the desorption of metal-containing fragments and compounds from a clean (sputtered, non-oxidized) surface at the ALE processing temperatures, it only suggests that these products may have already desorbed before the TPD experiment. The value of these observations is in the type of products that can be participating in ALE of this alloy. It is clear that this is a complex mixture, that oxygen presence is not necessarily detrimental and possibly useful in the ALE of the alloy, and that the balanced kinetics will have to include all the elements in a combination that does not change the concentration of these elements on a surface of the alloy. As also demonstrated in Fig. 4, boron can be removed from the surface as a chloride but also possibly as a mixed ligand compound, with a combination of acac and Cl ligands, which is consistent with the previous stability investigations of $B(acac)Cl_2$ compounds [43,44]. Thus, overall removal of all three elements from the CoFeB alloy follows the formation of products with overall formula $M(acac)_xCl_y$.

3.5. Investigation of ALE on a patterned sample containing CoFeB features, and the same features protected by a thin layer of MgO

To illustrate the efficiency of the proposed ALE with sequential exposure to chlorine and acacH for electronic devices, it was investigated on a more complicated patterned sample with CoFeB thin film layers deposited onto a silicon substrate and with selected areas of the alloy films protected by a thin film (~4 nm) of MgO. MgO was chosen as a protecting material based on its use in magnetic tunnel junctions. The sample was annealed at 440 K for 40 min followed by 30 ALE cycles of sequential exposure to chlorine and acacH. Following 30 ALE cycles, XPS imaging was performed on the resulting surface. Fig. 5 displays the schematic illustration of the patterned substrate, mapped image of the sample, and corresponding representative line profiles for Co, Fe, B, and Mg. The mapped image and the corresponding line profiles in Fig. 5

confirm the presence of MgO film covering selected structural features. As Mg 1s binding energy at 1303 eV may be affected by Cl Auger line (1304 eV), in this set of experiments Mg 2s binding energy (89 eV) was chosen to confirm the presence of magnesium based on survey spectra.

Furthermore, high resolution XPS was performed on the CoFeB alloy surface and on MgO surface before and after 30 ALE cycles to have a better understanding of the surface composition. As shown in column (a) of Fig. 6, there is no magnesium present on top of the alloy feature; however, cobalt, iron, and boron are all observed, and the change in concentration (or absence thereof) following ALE is consistent with previous XPS data described above. On the other hand, there is Mg 1s peak present on the MgO-protected feature shown in Fig. 6(b), which is slightly shifted to higher binding energy after ALE, this change is likely coupled with the presence of a small amount of chlorine. Since the thickness of MgO film is approximately 4 nm, the underlying CoFeB alloy thin film is also detectable on the MgO-protected alloy, albeit at much lower intensity, and as expected, no noticeable changes in corresponding spectral ranges are recorded following ALE.

Most importantly, the AFM study for the CoFeB/MgO patterned sample was used to confirm the selectivity of the proposed ALE mechanism to atomically etch CoFeB alloy over MgO thin films. As shown in Fig. 7a and 7b, the thickness the MgO-protected CoFeB thin film (the height of the corresponding step) was not changed following 30 ALE cycles. This step was measured to be 24.9 $\pm$ 0.5 nm before ALE and 24.4 $\pm$ 0.7 nm after 30 ALE cycles. However, at the CoFeB step, where the alloy is not protected by MgO, the thickness was decreased from 20.7 $\pm$ 0.6 nm to 16.6 $\pm$ 0.4 nm after ALE. This observation confirms that with the proposed etching process, MgO layer would not be etched while CoFeB alloy films is etched with $\sim$ 0.15 nm/cycle etch rate which is fully consistent with previous results.

4. Summary and conclusions

The key features of the mechanism of thermal atomic layer etching of CoFeB thin films were investigated using spectroscopic and microscopic techniques. It was shown that sequential exposures to chlorine and acetylacetone result in atomic layer etching of the alloy thin films with the etch rate that can be optimized to follow true ALE process: 0.15 nm/cycle. Although achieving an etching regime approaching ALE on an alloy would not be unexpected, using the same strategy on an alloy that has a light element, boron, was. TPD experiments showed that there are several products containing metals with both chlorine and acac ligands desorbing at the thermal regimes consistent with ALE. Microscopy studies confirm that by staying below 710 K, the surface remains smooth following ALE. The long time required for each cycle in these studies was needed because of the use of a solid-state electrochemical cell for chlorine dose. The modern industrial scale ALE setups will make the process much more efficient by using gaseous chlorine directly instead.

A thin layer of MgO was demonstrated to fully protect the CoFeB alloy from ALE, leading to the processing that can be used in real devices utilizing MTJs. In this work the approach with patterning the surface was only investigated to demonstrate the selectivity of etching at conditions optimized for a single material; however, it is easy to translate the same strategy to show the possibility of etching multiple materials and thus to pave the way for combinatorial approaches in ALE investigations.

CRediT authorship contribution statement

Mahsa Konh: Investigation, Methodology, Data curation, Writing – original draft. **Yang Wang:** Writing – review & editing. **Hang Chen:** Investigation, Writing – review & editing. **Subhash Bhatt:** Investigation, Writing – review & editing. **John Xiao:** Conceptualization, Methodology. **Andrew V. Teplyakov:** Conceptualization, Methodology, Data curation, Writing – review & editing.

Declaration of Competing Interest

The authors declare that they have no known competing financial interests or personal relationships that could have appeared to influence the work reported in this paper.

Acknowledgment

This work was supported by the National Science Foundation (CMMI2035354) and by the University of Delaware.

References

[1] B.H. McCarthy, S. Ponedal, IBM unveils world's first 2 nanometer chip technology, opening a new frontier for semiconductors, IBM News Room. (2021) 6–8.
[2] S.M. George, Y. Lee, Prospects for Thermal atomic layer etching using sequential, self-limiting fluorination and ligand-exchange reactions, ACS Nano. 10 (5) (2016) 4889–4894, https://doi.org/10.1021/acsnano.6b02991.
[3] A. Fischer, A. Routzahn, S.M. George, T. Lill, Thermal atomic layer etching: a review, J. Vac. Sci. Technol. A. 39 (3) (2021) 030801, https://doi.org/10.1116/6.0000894.
[4] K.J. Kanarik, T. Lill, E.A. Hudson, S. Sriraman, S. Tan, J. Marks, V. Vahedi, R. A. Gottscho, Overview of atomic layer etching in the semiconductor industry, J. Vac. Sci. Technol. A. 33 (2) (2015) 020802, https://doi.org/10.1116/1.4913379.
[5] S.M. George, Mechanisms of thermal atomic layer etching, Acc. Chem. Res. 53 (6) (2020) 1151–1160, https://doi.org/10.1021/acs.accounts.0c00084.
[6] A.D. Kent, D.C. Worledge, A new spin on magnetic memories, Nat. Nanotechnol. 10 (3) (2015) 187–191, https://doi.org/10.1038/nnano.2015.24.
[7] J. Grollier, D. Querlioz, K.Y. Camsari, K. Everschor-Sitte, S. Fukami, M.D. Stiles, Neuromorphic spintronics, Nat. Electron. 3 (7) (2020) 360–370, https://doi.org/10.1038/s41928-019-0360-9.
[8] I. Zutic, J Fabian, S.D. Sarma, Spintronics: Fundamentals and applications, Rev. Mod. Phys. 76 (2004) 323, https://doi.org/10.1103/RevModPhys.76.323.
[9] S.A. Wolf, J. Lu, M.R. Stan, E. Chen, D.M. Treger, The promise of nanomagnetics and spintronics for future logic and universal memory, Proc. IEEE. 98 (12) (2010) 2155–2168, https://doi.org/10.1109/JPROC.2010.2064150.
[10] M. Konh, A. Janotti, A. Teplyakov, Molecular mechanism of thermal dry etching of iron in a two-step atomic layer etching process: chlorination followed by exposure to acetylacetone, J. Phys. Chem. C. 125 (13) (2021) 7142–7154, https://doi.org/10.1021/acs.jpcc.0c10556.
[11] X. Lin, M. Chen, A. Janotti, R. Opila, In situ XPS study on atomic layer etching of Fe thin film using Cl_2 and acetylacetone, J. Vac. Sci. Technol. A. 36 (5) (2018) 051401, https://doi.org/10.1116/1.5039517.
[12] M. Konh, C. He, X.i. Lin, X. Guo, V. Pallem, R.L. Opila, A.V. Teplyakov, Z. Wang, B. o. Yuan, Molecular mechanisms of atomic layer etching of cobalt with sequential exposure to molecular chlorine and diketones, J. Vac. Sci. Technol. A. 37 (2) (2019) 021004, https://doi.org/10.1116/1.5082187.
[13] Z. Wang, R.L. Opila, In operando x-ray photoelectron spectroscopy study of mechanism of atomic layer etching of cobalt, J. Vac. Sci. Technol. A. 38 (2) (2020) 022611, https://doi.org/10.1116/1.5138989.
[14] Y. Kim, D. Shim, J. Kim, H. Chae, Thermal atomic layer etching of cobalt with Cl_2 plasma and hexafluoroacetylacetone (hfacH), ALD-ALE 2021 Conf. (2021). https://ald2021.avs.org/wp-content/uploads/2021/04/ALD-ALE-Virtual-Meeting-Overview.pdf.
[15] N.D. Altieri, J.-C. Chen, J.P. Chang, Controlling surface chemical states for selective patterning of CoFeB, J. Vac. Sci. Technol. A. 37 (1) (2019) 011303, https://doi.org/10.1116/1.5063662.
[16] X. Shan, J.J. Watkins, Kinetics of cuprous oxide etching with β-diketones in Supercritical CO_2, Thin Solid Films. 496 (2) (2006) 412–416, https://doi.org/10.1016/j.tsf.2005.08.274.
[17] E. Mohimi, X.I. Chu, B.B. Trinh, S. Babar, G.S. Girolami, J.R. Abelson, Thermal atomic layer etching of copper by sequential steps involving oxidation and exposure to hexafluoroacetylacetone, ECS J. Solid State Sci. Technol. 7 (9) (2018) P491–P495, https://doi.org/10.1149/2.0211809jss.
[18] N. Toyoda, K. Uematsu, Atomic layer etching by gas cluster ion beams with acetylacetone, Jpn. J. Appl. Phys. 58 (2019) 1–6, https://doi.org/10.7567/1347-4065/ab17c5.
[19] J.-C. Chen, N.D. Altieri, T. Kim, E. Chen, T. Lill, M. Shen, J.P. Chang, Directional etch of magnetic and noble metals. II. Organic chemical vapor etch, J. Vac. Sci. Technol. A. 35 (5) (2017) 05C305, https://doi.org/10.1116/1.4983830.
[20] F. Rousseau, A. Jain, L. Perry, J. Farkas, T.T. Kodas, M.J. Hampden-Smith, M. Paffett, R. Muenchausen, New approaches for dry etching metal oxides at low temperature and high rates, Mat. Res. Soc. Symp. Proc. 268 (1992) 57, https://doi.org/10.1557/PROC-268-57.
[21] J. Murdzek, S. George, Thermal atomic layer etching of cobalt using SO_2Cl_2 and P$(CH_3)_3$, ALD-ALE 2021 Conf. (2021). https://ald2021.avs.org/wp-content/uploads/2021/04/ALD-ALE-Virtual-Meeting-Overview.pdf.
[22] W. Xie, G.N. Parsons, Thermal atomic layer etching of metallic tungsten via oxidation and etch reaction mechanism using O_2 or O_3 for oxidation and WCl_6 as the chlorinating etchant, J. Vac. Sci. Technol. A. 38 (2) (2020) 022605, https://doi.org/10.1116/1.5134430.

[23] N.R. Johnson, S.M. George, WO_3 and W thermal atomic layer etching using "conversion-fluorination" and "oxidation-conversion-fluorination" mechanisms, ACS Appl. Mater. Interfaces. 9 (39) (2017) 34435–34447, https://doi.org/10.1021/acsami.7b09161.
[24] R. Sheil, J.M.P. Martirez, X. Sang, E.A. Carter, J.P. Chang, Precise control of nanoscale Cu etching via gas-phase oxidation and chemical complexation, J. Phys. Chem. C. 125 (3) (2021) 1819–1832, https://doi.org/10.1021/acs.jpcc.0c0893210.1021/acs.jpcc.0c08932.s00110.1021/acs.jpcc.0c08932.s002.
[25] B.M. Coffey, H.C. Nallan, J.G. Ekerdt, Vacuum ultraviolet enhanced atomic layer etching of ruthenium films, J. Vac. Sci. Technol. A. 39 (1) (2021) 012601, https://doi.org/10.1116/6.0000742.
[26] J.W. Clancey, A.S. Cavanagh, J.E.T. Smith, S. Sharma, S.M. George, Volatile etch species produced during thermal Al_2O_3 atomic layer etching, J. Phys. Chem. C. 124 (1) (2020) 287–299, https://doi.org/10.1021/acs.jpcc.9b06104.
[27] Y. Lee, S.M. George, Thermal atomic layer etching of Al_2O_3, HfO_2, and ZrO_2 using sequential hydrogen fluoride and dimethylaluminum chloride exposures, J. Phys. Chem. C. 123 (30) (2019) 18455–18466, https://doi.org/10.1021/acs.jpcc.9b04767.
[28] Y. Lee, S.M. George, Atomic layer etching of Al_2O_3 using sequential, self-limiting thermal reactions with $Sn(acac)_2$ and hydrogen fluoride, ACS Nano. 9 (2) (2015) 2061–2070, https://doi.org/10.1021/nn507277f.
[29] J. Zhao, M. Konh, A. Teplyakov, Surface chemistry of thermal dry etching of cobalt thin films using hexafluoroacetylacetone (hfacH), Appl. Surf. Sci. 455 (2018) 438–445, https://doi.org/10.1016/j.apsusc.2018.05.182.
[30] A.H. Basher, M. Krstić, K. Fink, T. Ito, K. Karahashi, W. Wenzel, S. Hamaguchi, Formation and desorption of nickel hexafluoroacetylacetonate $Ni(hfac)_2$ on a nickel oxide surface in atomic layer etching processes, J. Vac. Sci. Technol. A. 38 (5) (2020) 052602, https://doi.org/10.1116/6.0000293.
[31] S. Kondati Natarajan, M. Nolan, P. Theofanis, C. Mokhtarzadeh, S.B. Clendenning, In silico design of a thermal atomic layer etch process of cobalt, J. Vac. Sci. Technol. A. 39 (2) (2021) 022603, https://doi.org/10.1116/6.0000804.
[32] S.K. Song, J.-S. Kim, H.R.M. Margavio, G.N. Parsons, Multimaterial self-aligned nanopatterning by simultaneous adjacent thin film deposition and etching, ACS Nano. 15 (7) (2021) 12276–12285, https://doi.org/10.1021/acsnano.1c0408610.1021/acsnano.1c04086.s001.
[33] TaiZhe Lin, BaoTao Kang, MinHwan Jeon, C. Huffman, JeaHoo Jeon, SungJoo Lee, W. Han, JinYong Lee, SeHan Lee, GeunYoung Yeom, KyongNam Kim, Controlled layer-by-layer etching of MoS_2, ACS Appl. Mater. Interfaces. 7 (29) (2015) 15892–15897, https://doi.org/10.1021/acsami.5b03491.
[34] Casa XPS, Casa Software Ltd: Teignmouth, Uk (2010).
[35] M. Yasaka, X-ray thin-film measurement techniques, Rigaku J. 26 (2010) 1–9.
[36] M. Björck, G. Andersson, GenX (2007) 1174.
[37] S.D. Athavale, Realization of atomic layer etching of silicon, J. Vac. Sci. Technol. B 14 (1996) 3702, https://doi.org/10.1116/1.588651.
[38] A.I. Abdulagatov, V. Sharma, J.A. Murdzek, A.S. Cavanagh, S.M. George, Thermal atomic layer etching of germanium-rich SiGe using an oxidation and "conversion-etch" mechanism, J. Vac. Sci. Technol. A. 39 (2) (2021) 022602, https://doi.org/10.1116/6.0000834.
[39] H. Li, H. Li, W.-L. Dai, W. Wang, Z. Fang, J.-F. Deng, XPS studies on surface electronic characteristics of Ni-B and Ni-P amorphous alloy and its correlation to their catalytic properties, Appl. Surf. Sci. 152 (1-2) (1999) 25–34, https://doi.org/10.1016/S0169-4332(99)00294-9.
[40] T. Kim, Y. Kim, J.-C. Chen, J.P. Chang, Viable chemical approach for patterning nanoscale magnetoresistive random access memory, J. Vac. Sci. Technol. A 33 (2) (2015) 021308, https://doi.org/10.1116/1.4904215.
[41] D.R. Zywotko, J. Faguet, S.M. George, Rapid atomic layer etching of Al_2O_3 using sequential exposures of hydrogen fluoride and trimethylaluminum with no purging, J. Vac. Sci. Technol. A 36 (6) (2018) 061508, https://doi.org/10.1116/1.5043488.
[42] K.J. Kanarik, S. Tan, R.A. Gottscho, Atomic layer etching: rethinking the art of etch, J. Phys. Chem. Lett. 9 (16) (2018) 4814–4821, https://doi.org/10.1021/acs.jpclett.8b00997.
[43] I.V. Svistunova, E.V. Fedorenko, α-Substituted boron difluoride acetylacetonates, Russ. J. Gen. Chem. 78 (8) (2008) 1515–1523, https://doi.org/10.1134/S1070363208080094.
[44] O.B. Ryabchenko, L.A. Kuarton, I.V. Svistunova, V.I. Vovna, Modeling of the structure and IR spectra of boron difluoride acetylacetonate and its halogen-substituted derivatives, J. Struct. Chem. 58 (6) (2017) 1079–1089, https://doi.org/10.1134/S002247661706004X.